ADVANCING EARTH AND SPACE SCIENCES

Space Weather

RESEARCH ARTICLE
10.1029/2024SW004191

Special Collection:
Space Weather Events of 2024 May 9-15

Key Points:

- Magnetospheric and ionospheric analysis of storm sudden commencement using both satellites and ground magnetometers
- Effects of geomagnetically induced electric field during the sudden storm commencement of the geomagnetic storm
- Intense geoelectric fields observed at high latitudes only, due to the peculiar coronal mass ejection-shock inclination in the meridional plane

Correspondence to:
M. Piersanti,
mirko.piersanti@univaq.it

Citation:
Piersanti, M., Oliveira, D. M., D'Angelo, G., Diego, P., Napoletano, G., & Zesta, E. (2025). On the geoelectric field response to the SSC of the May 2024 super storm over Europe. *Space Weather*, *23*, e2024SW004191. https://doi.org/10.1029/2024SW004191

Received 1 OCT 2024
Accepted 26 JAN 2025

Author Contributions:
Conceptualization: M. Piersanti, D. M. Oliveira
Data curation: G. Napoletano
Formal analysis: M. Piersanti
Funding acquisition: P. Diego
Investigation: D. M. Oliveira, G. D'Angelo
Methodology: M. Piersanti
Writing – original draft: M. Piersanti
Writing – review & editing: D. M. Oliveira, G. D'Angelo, P. Diego, E. Zesta

On the Geoelectric Field Response to the SSC of the May 2024 Super Storm Over Europe

M. Piersanti[1,2,3], D. M. Oliveira[4,5], G. D'Angelo[1,2], P. Diego[2], G. Napoletano[1], and E. Zesta[5]

[1]Department of Physical and Chemical Sciences, University of L'Aquila, L'Aquila, Italy, [2]INAF-IAPS, Rome, Italy, [3]INFN - Sezione di Roma "Tor Vergata", via della ricerca scientifica, Rome, Italy, [4]Goddard Planetary Heliophysics Institute, University of Maryland, Baltimore, MD, USA, [5]Geospace Physics Laboratory, NASA Goddard Space Flight Center, Greenbelt, MD, USA

Abstract Solar variability can lead to significant disturbances, such as coronal mass ejections (CMEs). A CME impacting the Earth's magnetosphere often causes geomagnetic storms that affect not only the magnetosphere but also the ionosphere, the upper atmosphere, and even the ground. During extreme events, rapidly changing geomagnetic fields can create strong geomagnetically induced currents (GICs) at ground. These GICs can severely impact human technology, causing damage to high-voltage power transformers and leading to power outages, as well as corrosion in oil and gas pipelines. On 10 May 2024, the most intense geomagnetic storm since the Halloween 2003 storm impacted Earth's environment, causing auroras to appear at much lower latitudes than usual in both the northern and southern hemispheres. This study investigates the effects of geomagnetically induced electric fields (GIEs), and hence GICs, during the sudden storm commencement (SSC) of the geomagnetic storm on 10 May 2024, over Europe, using the European quasi-Meridional Magnetometer Array ground magnetometers. Despite the magnetometer array being placed in the late afternoon (18:00 LT), the combined influence of a strong solar wind dynamic pressure amplitude ($P \sim 22nPa$) and a significant, long-lasting southward interplanetary magnetic field (IMF) ($B_{z,IMF} \sim -25$nT) resulted in strong SSC amplitudes (~180nT) at mid-low latitudes ($\lambda \sim 57°$N). Results suggest that the CME-driven shock inclination in the meridional plane leads to high GIE driven only at high latitudes. In addition, the decomposition of the SSC disturbance field at ground into ionospheric (DP field) and magnetospheric (DL field) origin contribution should commend input to GIEs (and hence to GICs) from both DL and DP fields, rather than ionospheric current alone.

Plain Language Summary Changes in the sun's activity can cause major disruptions, like coronal mass ejections (CMEs). When a CME hits Earth's magnetic field, it can trigger geomagnetic storms that affect not just the magnetic field but also the ionosphere and the ground. During extreme events, rapidly changing magnetic fields can create strong currents on the ground, known as geomagnetically induced currents (GICs). These GICs can damage technology, such as high-voltage power transformers, leading to power outages and corrosion in pipelines. On 10 May 2024, the most intense geomagnetic storm since the Halloween 2003 storm hit Earth, causing auroras to appear much farther south than usual in both hemispheres. This study looks at the effects of GICs during the start of the storm at 17:05 UT, in Europe. We found that the combination of strong solar wind pressure, a significant, long-lasting southward interplanetary magnetic field, and the angle of the CME-driven shock resulted in high GIC values.

1. Introduction

Coronal mass ejections (CMEs) are the most geoeffective solar disturbances (Crooker et al., 1997; Shen et al., 2017), that whether impacting Earth's magnetosphere causes a storm sudden commencement or sudden impulse (SSC or SI). CMEs typically carry magnetic clouds with intense interplanetary magnetic fields (IMFs), whose north-south component $\left(B_{z,IMF}\right)$ rotates rapidly during interplanetary travel (Crooker et al., 1997; Shen et al., 2017). If $B_{z,IMF}$ is directed southward when interacting with Earth's northward geomagnetic field, it can trigger a reconnection process (W. Gonzalez et al., 1994; Souza et al., 2017; Piersanti et al., 2017). The energy transferred during this process depends on how long $B_{z,IMF}$ remains southward (W. Gonzalez et al., 1994; W. D. Gonzalez et al., 1999), potentially leading to a geomagnetic storm (W. Gonzalez et al., 1994; W. D. Gonzalez et al., 1999; Piersanti et al., 2017). SSC is a rapid increase in magnetic field strength detected both in the magnetosphere and at ground, resulting from an increase in the magnetopause current due to magnetopause compression (e.g., Piersanti & Villante, 2016; Villante & Piersanti, 2008, 2009, 2011), induced by a shock wave from the CME leading edge (Araki & Shinbori, 2016; Lugaz et al., 2015). Furthermore, SSCs play a crucial role in various aspects of solar-terrestrial physics and space weather, including the compression of the magnetosphere, the acceleration and transport of energetic particles, and the precipitation of charged particles in the dayside auroral zone (Boudouridis et al., 2003; Feldstein et al., 1997; Tsurutani et al., 2001).

In experimental observations, SIs are typically identified by an increase in the geomagnetic fields, occurring over a period of approximately two to fifteen minutes and a transition between two steady states. On the ground, the geomagnetic response is currently interpreted through the combined contributions of magnetospheric (typically the magnetopause) and ionospheric currents (Araki, 1994; Rastogi, 1978). The SSC amplitude on the ground strictly depends on geomagnetic latitudes and local times (Araki, 1977; Matsushita, 1962). Here, the total disturbance field (D_{SI}), representing the variation of the geomagnetic field at ground associated to the passage of the IPs, can be broken down into different subfields, specifically $D_{SI} = DL + DP$, where: the DL field ("L" stands for "low latitude") is a step-like structure of magnetospheric origin, which is dominant at low latitudes; and DP field ("P" stands for "polar latitude") is a double pulse structure of ionospheric origin, which is dominant at high latitudes. The first pulse is known as the preliminary impulse (PI), and the second pulse is known as the main impulse (MI). Based on Araki (1994)'s model, the enhancement of solar wind (SW) pressure increases the magnetopause current, resulting in a step-like increase with the greatest amplitude at the equator. A two-cell ionospheric current (DP two-type currents), induced by a dusk-to-dawn electric field along the compressional wave front, generates the PI. If the SW dynamic pressure remains high, the magnetospheric convection adjusts to the compressed state, forming a new ionospheric vortex system (opposite to the PI), which corresponds to the MI. This MI is driven by an electric field originating in the polar region and is transmitted from the outer magnetosphere through field-aligned currents (FACs) that flow into the ionosphere in the morning and out in the afternoon (Iijima & Potemra, 1976). At low latitudes, the DP field is characterized by a positive variation in the H (H being the north-south component of the magnetic field at ground observed in the geomagnetic reference frame (Laundal & Richmond, 2017)) component, with its amplitude peaking around local noon, and a negligible or null variation in the D (D being the east-west component in the geomagnetic reference frame (Laundal & Richmond, 2017)) component. Tsunomura (1998) demonstrated that at middle and low latitudes, variations in the H component are accompanied by clear negative variations in the D component, which are attributed to the influence of ionospheric current systems. Additionally, Villante and Piersanti (2009, 2011), through the analysis of 55 SI events, suggested that both magnetospheric and ionospheric currents concurrently influence the H and D components. Based on these results, Piersanti and Villante (2016) developed a model able to correctly discriminate between the magnetospheric and ionospheric contributions to SI/SSC detected on the ground using both the H and D magnetic field components. In addition, they were able to correctly assess the ionospheric current vortices developing during the SI/SSC occurrence.

In this scenario, it is worth noting that severe solar disturbances can damage modern technology, such as telecommunications, power grids, and oil pipelines. On the ground, one of the main hazard during a geomagnetic storm is geomagnetically induced currents (GICs). These currents result from the induction of an electric field on the Earth's surface by rapid variations in the magnetosphere and ionosphere currents (Pirjola, 2000, 2002; Pulkkinen et al., 2012; Viljanen & Pirjola, 1994). Although GIC effects are typically more evident at higher latitudes (Ngwira et al., 2015; Oliveira et al., 2024; Pulkkinen et al., 2012; Viljanen & Pirjola, 1994; Viljanen et al., 2004), recent research indicates that low-latitude and equatorial regions can also be significantly affected (e.g., Carter et al., 2015, 2016; Liu et al., 2018; Mac Manus et al., 2017; Marshall et al., 2017; Ngwira et al., 2013; Rodger et al., 2017). Piersanti et al. (2019) introduced a model (MAgnetospheric Ionospheric and Geomagnetically Induced Current - MA.I.GIC.) able to correctly evaluate the geoelectric field from ground magnetometer observations.

In this paper, we analyze the effects of GICs during the SSC of the geomagnetic storm on 10 May 2024, over Europe, using European quasi-Meridional Magnetometer Array (EMMA) ground magnetometers. We start analyzing the solar wind parameters, then we move into the magnetosphere trying to identify the principal magnetospheric current system amplified by the interplanetary shock arrival, and finally we made a deep analysis of the ground response in terms of both magnetic and electric field. The paper is organized as follows: Section 2 describes the data sets used; Section 3 shows the analysis of the interplanetary conditions; Section 4 presents the results in the magnetospheric medium; Section 5 shows the analysis on the ground; in the last two sections we discuss the results and make the conclusions.

2. Data Sets

In this work, we used SW parameter and IMF data collected by the Deep Space Climate Observatory (DSCOVR) satellite (Loto'aniu et al., 2022). DSCOVR serves as the successor to NASA's ACE spacecraft, continuing the task of monitoring solar wind near the L1 point upstream of Earth, in the frame of the space weather context. The IMF data used in this study were collected by the MAG magnetometer onboard DSCOVR. The SW parameter data, namely solar wind velocity, density, and temperature, were collected by the Faraday Cup instrument onboard DSCOVR. Both DSCOVR data sets used in this study have a resolution of 1 min (Loto'aniu et al., 2015). DSCOVR data used in this study are represented in geocentric solar ecliptic (GSE) coordinates. Data processing techniques are explained by Oliveira (2023b).

We used data from the Geostationary Operational Environmental Satellite (GOES) that is a system of geostationary satellites managed by NOAA in collaboration with NASA. The satellites are positioned at 6.6 R_E (R_E being the Earth radius) altitudes to collect data useful for weather and space weather forecasting. In this work we used GOES_{16} and GOES_{18} that are located at a longitude of 75°W and 137°W, respectively. Magnetic field observations are sampled at 1 min and are referred to the GSE coordinate system (Loto'aniu et al., 2019; Loto'aniu et al., 2023).

Global geomagnetic index data were provided by the SuperMAG initiative (Gjerloev, 2009). Geomagnetic activity is represented by the SuperMAG partial ring current index (Newell & Gjerloev, 2012), and by the SuperMAG auroral electrojet indices SMU and SML (Newell & Gjerloev, 2011), with SME = SMU − SML. The SME and SMR indices are similar to the traditional AE = AU − AL and SYM-H indices (AE and SYM-H being the high latitude auroral electrojet and mid latitude geomagnetic disturbance indices, respectively), but more stations at high latitudes (SME) and mid/low latitudes (SMR) are used to compute the indices. All SuperMAG indices data used in this study have a resolution of 1 min. Techniques used to derive the SuperMAG indices are described by Gjerloev (2012).

For local geomagnetic activity, we use ground magnetometer data from the INTERMAGNET array (St-Louis, 2020). The INTERMAGNET data provided by individual stations have cadence of 1 min.

We use data from EMMA. Established in 2012 as part of the PLASMON FP7 European project (Lichtenberger, János et al., 2013). EMMA consists of 27 stations (see Table 1), formed through the consolidation and expansion of existing European magnetic arrays, including South European GeoMagnetic Array (SEGMA), Magnetic Meridian 100 (MM100), and the Finnish segment of International Monitor of Auroral Geomagnetic Effects (IMAGE) (Vellante et al., 2014).

Both INTERMAGNET and EMMA magnetic field data are reported in the geomagnetic reference frame, where H is along the geomagnetic north-south direction, D is along the east-west direction and Z complete the coordinate system (Laundal & Richmond, 2017).

3. Interplanetary Observations

Figure 1 shows SW parameters and IMF at the moment of the IP shock arrival at DSCOVR. Upstream (non-shocked) and downstream (shocked) regions are defined in a time window of 5–10 min around the shock onset, occurring at 17:05 UT (here the SW data have been propagated from DSCOVR position down to the Earth's magnetopause). Clear compression states of SW parameters and IMF by the shock are shown by the ratio of the parameter after (downstream region) to before (upstream region) for IMF magnitude B ($8.6nT$); SW number density N (6.9 cm^{-3}); and SW dynamic pressure $P_d = \rho V^2$ ($14.8nPa$). These compression ratios indicate that the shock was stronger than average shocks (Oliveira, 2023b). However, it is noticeable that these parameters do not enhance sharply as they occur for very fast and nearly frontal shocks (Oliveira, 2023a). Therefore, these gradual enhancements of SW parameters and IMF suggest that the shock of 10 May 2024 did not hit the magnetosphere nearly head-on.

Computation of the shock parameters, including shock impact angles and speeds, are performed with the Rankine-Hugoniot (RH) jump conditions. These conditions are expressed by equations that account for conservation of energy and momentum across the shock surface, and conservation of tangential electric field parallel to the shock surface (Kennel et al., 1989; Priest, 1981).

Table 1
EMMA Stations Location in Terms of Geographic and Geomagnetic (CGM) Latitude, Longitude, Magnetic Local Time (MLT), and Country

Code	Name	Geo lat (°)	Geo long (°)	MLat	MLT	Country
KEV	Kevo	69.76	27.01	66.30	20.93	Finland
MAS	Masi	69.46	23.70	66.16	21.12	Finland
KIL	Kilpisjärvi	69.06	20.77	65.91	21.29	Finland
IVA	Ivalo	68.56	27.29	65.07	20.97	Finland
MUO	*Muonio*	68.02	23.53	64.70	21.19	Finland
SOD	Sodankylä	67.37	26.63	63.90	21.05	Finland
PEL	Pello	66.90	24.08	63.54	21.21	Finland
RAN	Raniu	65.90	26.41	62.41	21.12	Finland
OUJ	Oulujärvi	64.52	27.23	60.97	21.13	Finland
MEK	Mekrijärvi	62.77	30.97	59.05	20.97	Finland
HAN	Hankasalmi	62.25	26.60	58.65	21.23	Finland
NUR	Nurmijärvi	60.50	24.65	56.88	21.39	Finland
TAR	Tartu	58.26	26.46	54.46	21.34	Finland
BRZ	Birzai	56.21	24.75	52.31	21.48	Lithuania
HLP	Hel	54.61	18.81	50.69	21.87	Poland
SUW	Suwalki	54.01	23.18	49.95	21.62	Poland
BEL	Belsk	51.83	20.80	47.56	21.80	Poland
PPN	Polesie National Park	51.45	23.13	47.12	21.67	Poland
VYH	Vyhne	48.49	18.84	43.75	21.97	Slovakia
HRB	*Hurbanovo*	47.87	18.18	43.02	22.02	Slovakia
WIC	*Conrad Observatorium*	47.55	15.52	42.64	22.19	Austria
NCK	*Nagycenk*	47.63	16.72	42.73	22.11	Hungary
THY	Tihany	46.90	17.89	41.88	22.05	Hungary
THO	*Thoiry*	46.24	05.97	41.13	22.81	France
CST	*Castello Tesino*	46.05	11.65	40.83	22.45	Italy
LOP	*Lonjsko Polje*	45.41	16.66	40.09	22.15	Croatia
RNC	Ranchio	43.97	12.08	38.26	22.45	Italy
AQU	L'Aquila	42.38	13.32	36.29	22.39	Italy

Note. Stations highlighted in italic were not available for the 10 May 2024 SSC event.

The framework used for computation of shock parameters and properties is outlined by Oliveira (2023b). The RH conditions are used to compute the shock speed v_s, the shock impact angle θ_{x_n}, defined as the angle between the shock normal vector and the GSE x-line, and φ_{y_n}, the clock angle the shock normal vector performs with the y-axis in the yz plane. As explained by Oliveira (2023a), since data are represented in GSE coordinates, $\theta_{x_n} = 180°$ indicates a purely frontal shock, whereas an inclined shock is indicated by shock normals with $90° < \theta_{x_n} < 180°$. We then obtain $v_s = 661.58$ km/s, $\theta_{x_n} = 142.04°$, and $\varphi_{y_b} = 96.64°$. Therefore, the 10 May 2024 shock was a strong shock with moderate inclination with respect to the x-line and had its shock normal linearly aligned with the meridional xz plane. This is explained by the unusually high solar wind V_z component as seen in Figure 1. The implications of this unusual shock inclination to our results will be discussed later in this work.

4. Magnetospheric Observations

Figure 2 shows the variation of the magnetosphere in red as evaluated using the TS04 model (N. A. Tsyganenko & Sitnov, 2005) after the IP shock arrival at Earth on 10 May 2024 at 17:05 UT (blue dashed line). It is apparent that the magnetopause is located at about 10 R_E upstream from Earth before the shock arrival (black lines), but during

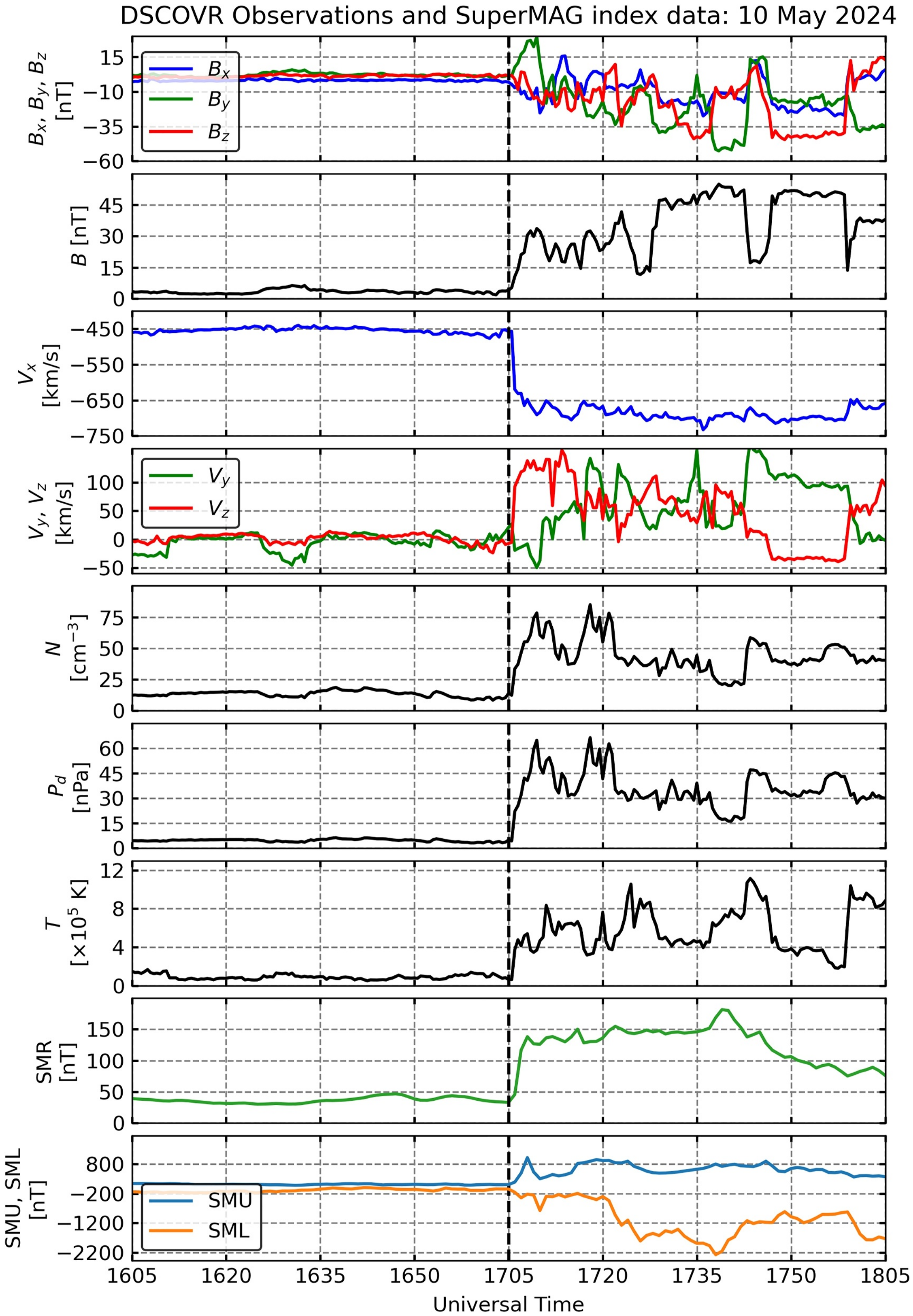

Figure 1. Solar wind parameters, IMF, and SuperMAG geomagnetic indices data before and after the IP shock of 10 May 2024. From top to bottom: the three components of the IMF; IMF magnitude; V_x component of the solar wind velocity; V_y and V_z components of the solar wind velocity; solar wind ion number density; solar wind ram pressure $\left(P_d = \rho V^2\right)$; solar wind temperature; SuperMAG partial ring current index; and SuperMAG SMU and SML indices.

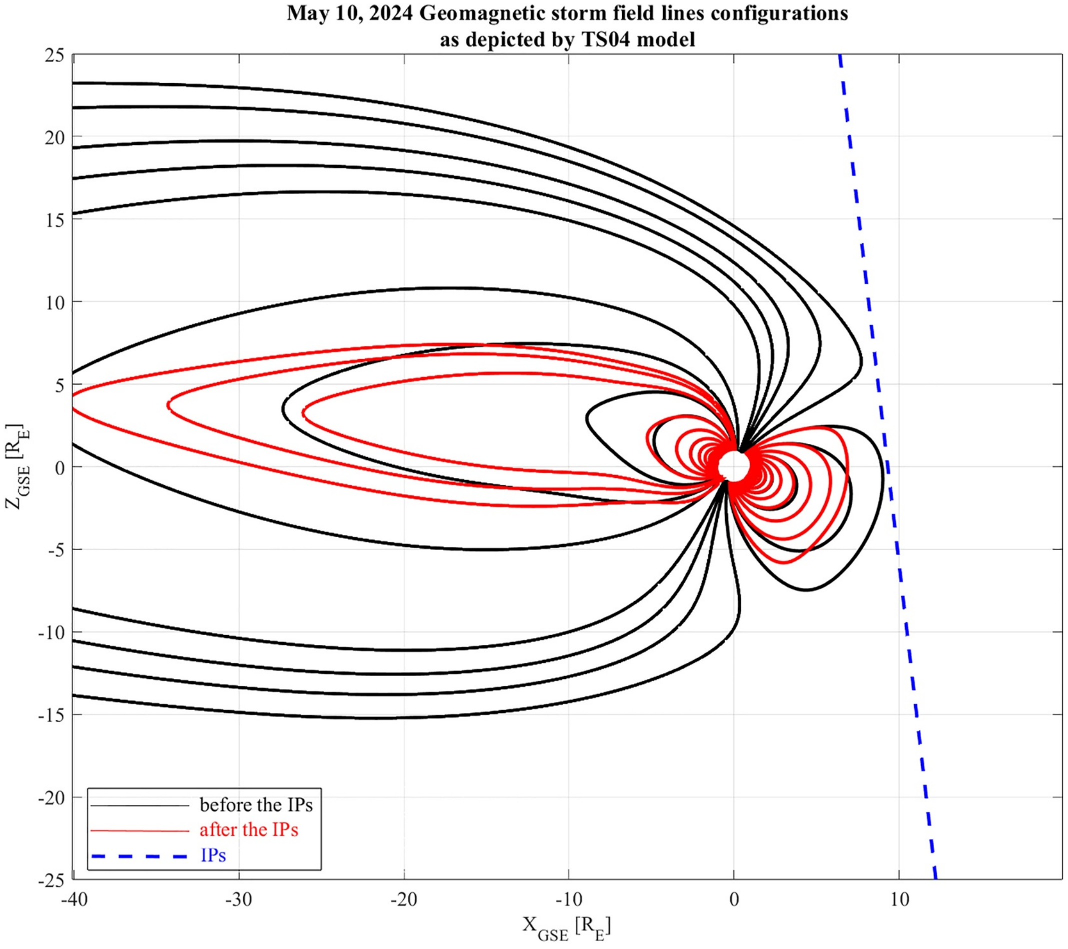

Figure 2. Magnetospheric field lines configurations as depicted by the TS04 model before (black lines) and after (red lines) the IPs arrival (blue dashed line).

shock driving conditions, it is quite compressed and the stand-off distance is reduced to less than 6.5 R_E. In addition, the model expected a strong compression of magnetospheric field lines, most likely caused by the strong SW parameters, southward IMF and IMF compression ratios shown in Section 3 (Lockwood, Mike et al., 2020).

In order to understand the role played by the different magnetospheric current systems during the IPs passage, we compare the data measured by $GOES_{16}$ and $GOES_{18}$, which were located in the noon (LT = 12:05) and in the morning sectors (LT = 08:05) respectively, with a modified TS04 model (hereafter TS04*), using the technique described in Piersanti et al. (2022). In this case, in order to obtain the best magnetospheric field representation at both satellites, we only considered the action of the magnetopause current plus the ring current (Villante & Piersanti, 2008). The results are shown in Figure 3. It can be easily seen that the TS04* (red dashed lines) well reproduces the $GOES_{18}$ satellite observations (right panels, blue line), while it fails in replicating the $GOES_{16}$ measurements (left panels, blue lines). In particular, for the $B_{z,GSE}$ component (bottom left panel), the model and the data exhibit opposite behavior. In fact, while TS04* shows a rise in the magnetospheric field, as expected by an increase in the magnetopause and ring currents induced by positive SW ΔP, geosynchronous magnetic observations present a positive (~1 minute longer) and then a strong $\left(\Delta B_{z,GSE} \sim 180nT\right)$ negative variation. Such an experimental observation can be explained in terms of the variation of the IMF B_z component behavior driving the position of the sub-solar point of the magnetopause (Bonde et al., 2018). In fact, at $GOES_{16}$, $\Delta B_{z,GSE} > 0$ occurs in correspondence of positive IMF B_z, while $\Delta B_{z,GSE} < 0$ occurs during IMF $B_z < 0$. This condition, characterized by the huge negative amplitude of the IMF $\left(B_z \sim -30nT\right)$, brought the standoff position of the magnetopause to a distance of less than 6.5 R_E, which is lower than the radius of the geosynchronous orbit. As a

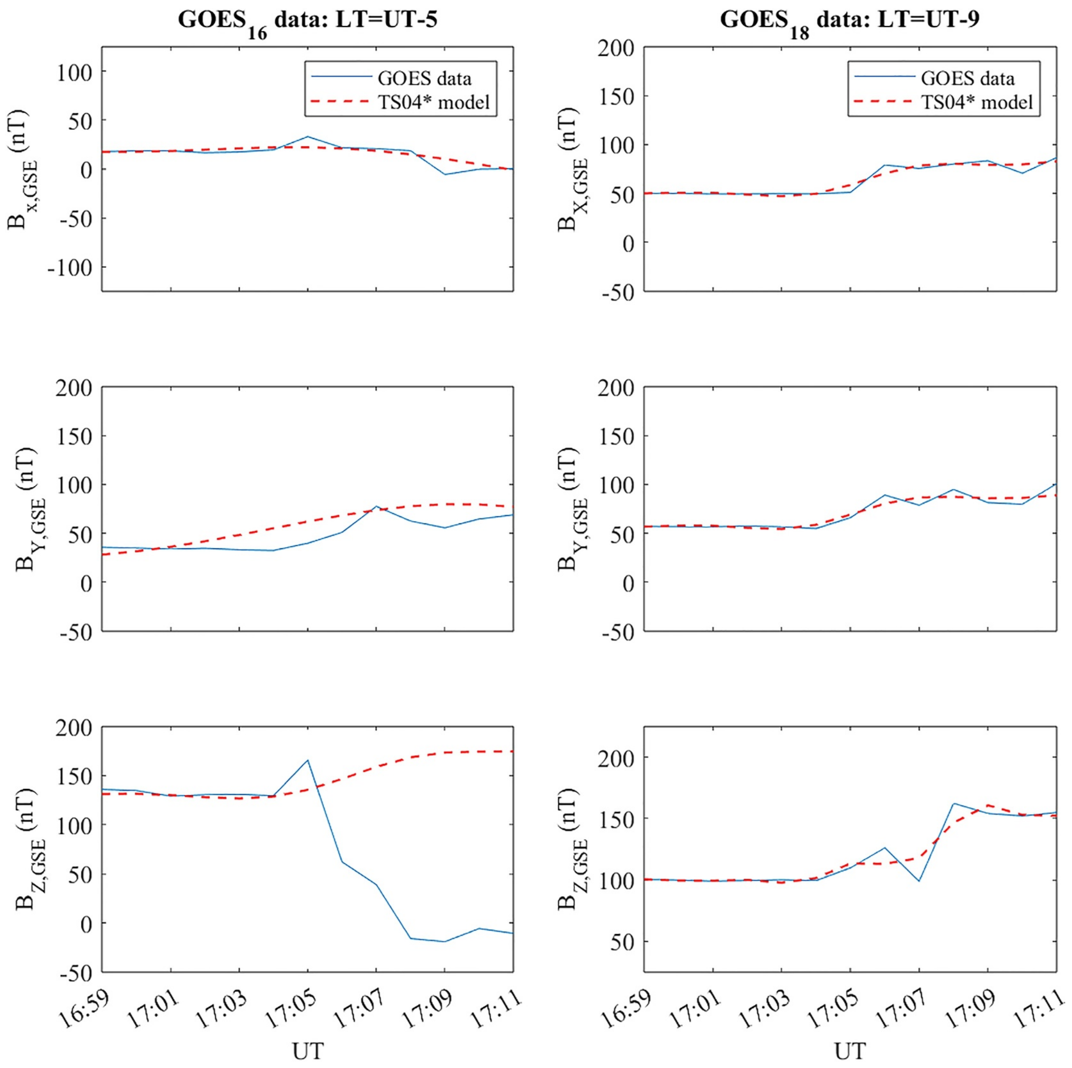

Figure 3. GOES observations (blue lines) versus TS04* model previsions (red dashed lines). Left and right panels show GOES$_{16}$ and GOES$_{18}$ magnetic field observations, respectively. Upper panels reports the X component, middle panels reports the Y component and Lower panels reports the Z component along the GSE reference frame. For both satellites magnetospheric field previsions, in the TS04* model, the concurrent contribution of magnetopause and ring current has been considered.

consequence, $GOES_{16}$ satellite, which was located close to the local noon, at 17:08 UT crossed the magnetopause (i.e. when $B_{z,GSE}$ cross 0) and moved out into the interplanetary space.

A different situation occurred for $GOES_{18}$, which was located in the local morning sector. In fact, here the TS04* model was able to well reproduce the observations along all the three components, confirming the key role played by both the magnetopause and ring currents in driving the magnetospheric field variations during a SSC. This outcome agrees with the statistical results obtained by Villante and Piersanti (2011) and by Lee and Lyons (2004). We want to mention that we tried to discriminate between the partial and symmetric part of the ring current in our TS04* simulation. What we obtained (not shown) is that the partial ring current only gives a very small boost (~ 2 nT on average) to the variation of the magnetospheric field driven by the IPs arrival.

5. Ground Observations and Geoelectric Field Evaluation

Figure 4 shows INTERMAGNET northward magnetic field component data (H) recorded in both hemispheres by eight different stations at different magnetic local times (MLTs) and magnetic latitudes (hereafter, λ). In all panels, the blue lines show northern hemisphere data, and the red lines southern hemisphere data. Top left panel

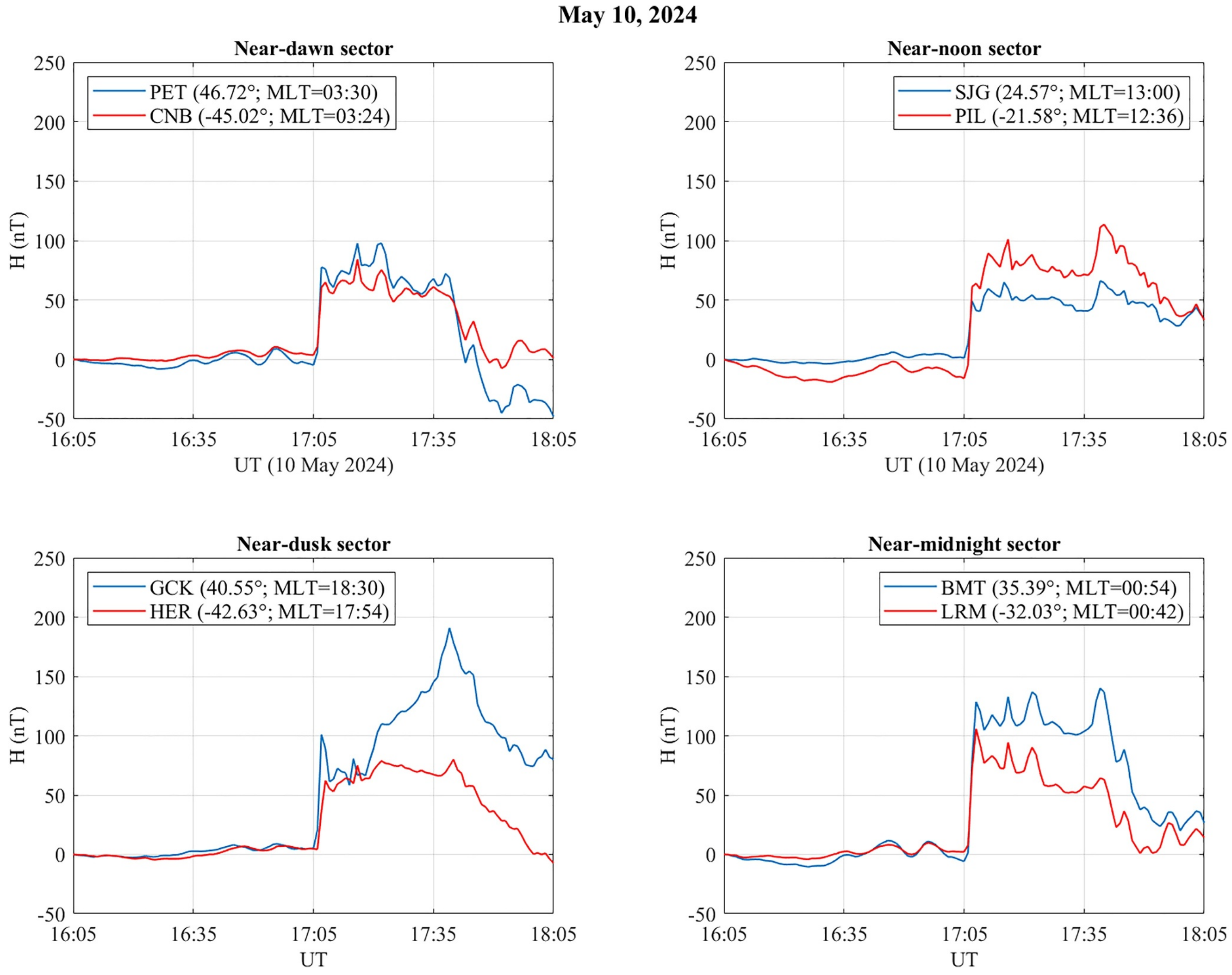

Figure 4. INTERMAGNET ground magnetometer observations in response to the SSC on 10 May 2024. Top left, near-dawn sector, Paratunka (PET) and Canberra (CNB); top right, near-noon sector, San Juan (SJG) and Pilar (PIL); lower left, near-dusk sector, Grocka (GCK) and Hermanus (HER); and lower right, near-midnight sector, Beijing Ming Tombs (BMT) and Learmonth (LER). The data shown in the legends represent magnetic latitudes (in degrees) and magnetic local times (hours). Data of stations in the northern hemisphere are represented in blue, and in the southern hemisphere, in orange. In each plot time length is 2 hr, 1 before and 1 after the SSC occurrence.

shows data from near-dawn stations Paratunka (PET, $\lambda = 46.6°$, MLT = 03:30) and Canberra (CNB, $\lambda = -44.9°$, MLT = 03:24); Top right panel, near-noon stations, San Juan (SJG, $\lambda = 24.6°$, MLT = 13:00) and Pilar (PIL, $\lambda = -21.6°$, MLT = 12:36); Bottom left panel, near-dusk stations Grocka (GCK, $\lambda = 40.6°$, MLT = 18:30) and Hermanus (HER, λ = -42.6°, MLT = 17:54); Bottom right panel, near-midnight stations BMT (Beijing Ming Tombs, $\lambda = 35.4°$, MLT = 00:54) and LRM (Learmonth, $\lambda = -32.0°$, and MLT = 00:42). A baseline based on the previous quite day was subtracted from the data for a coarse comparison. The shock impacted the magnetosphere at 17:05 UT on 10 May 2024. These stations were chosen because their magnetic latitudes are away from the auroral and equatorial electrojet currents.

As clearly shown in the figure, in the near-dawn, -dusk, and -midnight MLT regions, the northern hemisphere stations show larger SSCs in comparison to their southern hemisphere counterpart stations, except for the near-noon sector. These observations are consistent with our results regarding the shock impact angle, meaning that the shock had a moderate inclination in the xz meridional plane. Consequently, since the shock normal vector had a minor inclination in the azimuthal direction, the shock impacted the northern magnetosphere first, as depicted in Figure 2. The exception observed in the near-noon sector is seen in the larger H component observed by PIL compared to SJG. This effect can be explained by the fact that PIL is located deep within the Southern Atlantic Anomaly (SAA), where the geomagnetic field is the weakest on the planet (Trindade et al., 2018). Since the geomagnetic field at PIL is weak, its relative response to the shock compression is larger than the relative response of stronger fields in other regions of the planet, including SJG. This occurs because the relative response of a weak magnetic field is larger than the relative response of a strong magnetic field with respect to a similar driver.

Figure 5 illustrates the magnetic field observations along EMMA during the SSC. During the period under investigation, 21 stations were operational (see Table 1). At 17:05:16 UT, all stations recorded the SSC in both the H (black lines) and D (red dashed lines) components. As predicted by Araki (1994), the SSC behavior varies significantly with the magnetic latitude of the observatory (EMMA was in the local afternoon sector) and exhibits the following characteristics:

- Low magnetic latitudes ($36° < \lambda < 44°$): The H and D components show sudden positive and negative variations, respectively. Interestingly, before stabilizing at 17:10:58 UT, H and D reach a maximum and minimum value at 17:08:35 UT. Variations between the pre- and post-SSC steady states, as well as the pre-SSC and maximum/minimum (H/D) values, increase with magnetic latitude.
- Middle magnetic latitudes ($47° < \lambda < 60°$): Similarly to lower magnetic latitudes, but both horizontal components exhibit small amplitude preliminary reverse impulses (PRI, Araki, 1994) for H and preliminary positive impulses (PPI, Araki, 1994) for D, peaking at 17:06:35 UT and increasing with magnetic latitude.
- High magnetic latitudes ($60° < \lambda < 64°$): Both H and D components display similar characteristics to lower magnetic latitudes but with a broader increase. Interestingly, Pc1-2 ultra low frequency (ULF) waves appear to be superimposed on the north-south magnetic signal during the SSC's rising phase (Olson & Lee, 1983).
- Polar magnetic latitudes ($\lambda > 64°$): Both H and D components show PRI and PPI, respectively, with amplitudes increasing with magnetic latitude. Pc4-5 wave activity is clearly observed along the H component shortly after the SSC occurrence (from 17:11 UT) (D. Zhang et al., 2020).

We applied the Piersanti and Villante (2016) model to assess both the DL and DP fields along the H and D components. Figure 6 shows three examples of the results for low (AQU - $\lambda = 36.29°$, $MLT = 15:29$), middle (BEL - $\lambda = 47.56°$, MLT = 15:00) and high (MAS - $\lambda = 66.16°$, MLT = 14:14) magnetic latitude sample stations, showing north-south (upper panels) and east-west (lower panels) components. In these figures, black lines represent the DL field, red lines represent the DP field, and blue lines indicate the magnetic observations.

- Low magnetic latitudes (left panels): The H component shows a positive DL field, while the D component shows a negative DL field, with amplitudes around 100 and 30 nT, respectively. The DP field displays clear negative PI and positive MI along the H component, and positive PI and negative MI along the D component, with amplitudes of approximately 30 nT (PI) and 40 nT (MI) for H, and 10 nT (PI) and 20 nT (MI) for D.
- Middle magnetic latitudes (middle panels): The characteristics are similar to those at lower latitudes, but both DL and DP fields exhibit higher amplitudes along H, while DL field of D component becomes smaller.
- High/polar magnetic latitudes (right panels): The DL field shows lower amplitude values along H, while DL field of D component gets larger. However, the DP field displays large negative PI (around 100 nT) and significant positive MI (around 150 nT) along the H component. The D component shows high amplitude positive PI (around 50 nT) and large negative MI (around 70 nT).

Figure 7 illustrates the variations of the DL and DP fields as a function of the magnetic latitude. The amplitude of both disturbance fields has been calculated considering both the H and D components (quadratic sum). The DL field (left panel) shows a significant increase up to 62° latitude, followed by a rapid decrease. Its maximum value (approximately 160 nT) is observed at RAN ground station ($\lambda = 62.41°$). The DP field exhibits a similar pattern for both the PI (top-right) and MI (bottom-right). Both PI and MI increase with magnetic latitude up to $\lambda \sim 65°$, then decrease.

To measure the possible impact of the SSC on technological infrastructures, we applied the MA.I.GIC. model (Piersanti et al., 2019) for the computation of the geoelectric field that can provide an idea of GICs intensity. The geoelectric field is calculated using magnetic field data taken along EMMA ground stations. Figure 8 shows an example of the geoelectric field (E) evaluated at three sample geomagnetic observatories at lowest, middle and highest EMMA magnetic latitudes, namely: AQU ($\lambda = 36.29°$), BEL ($\lambda = 47.56°$) and MAS ($\lambda = 66.16°$). It can be easily seen that the E amplitudes increase with magnetic latitudes, as expected (Pulkkinen et al., 2012;

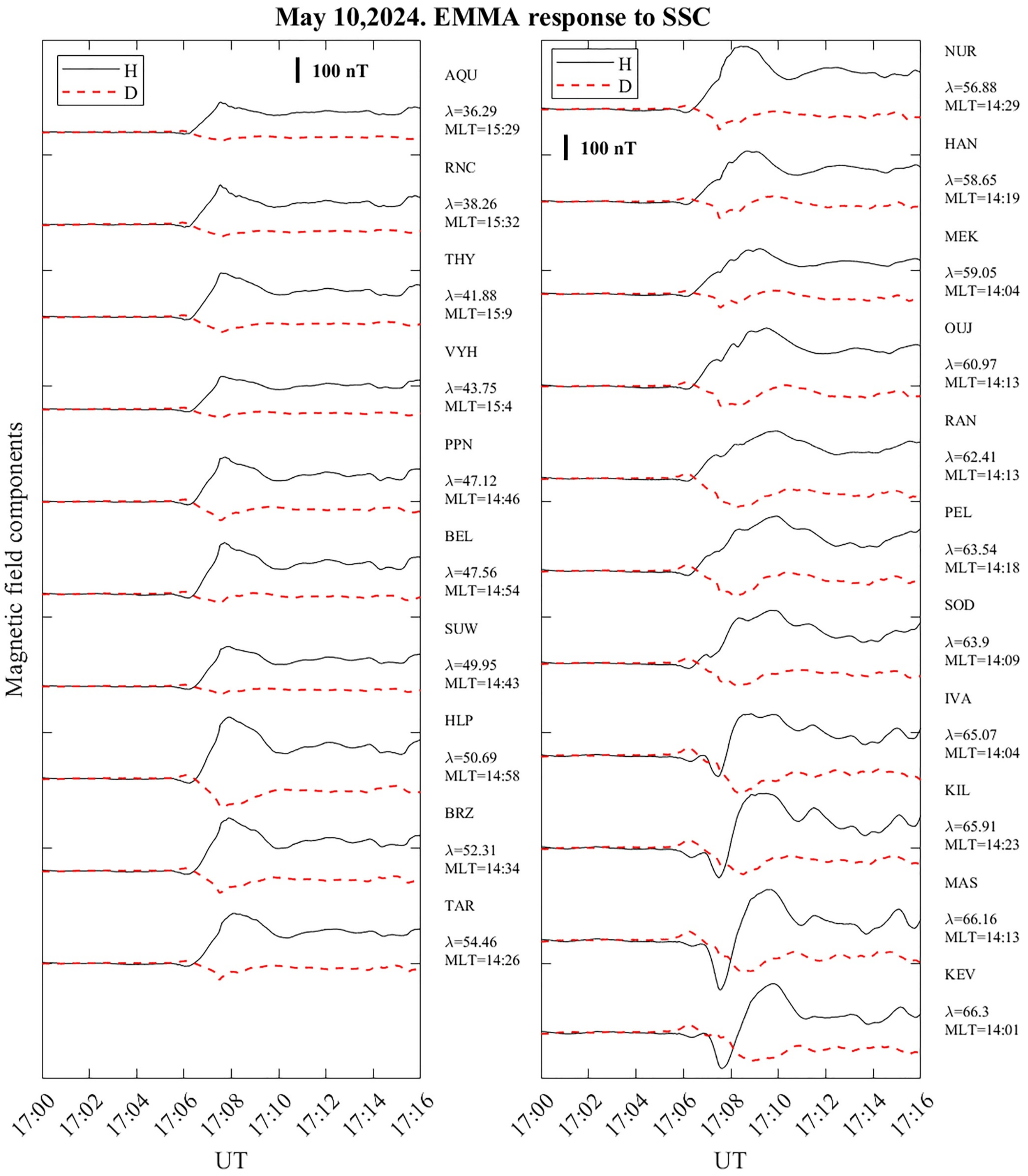

Figure 5. Magnetic field observations along EMMA stations during the SSC occurrence. Stations are ordered from the lowest (AQU, top-left) to the highest (KEV, bottom-right) magnetic latitudes (λ). Black and red traces are representative of the H and D component of the geomagnetic field, respectively.

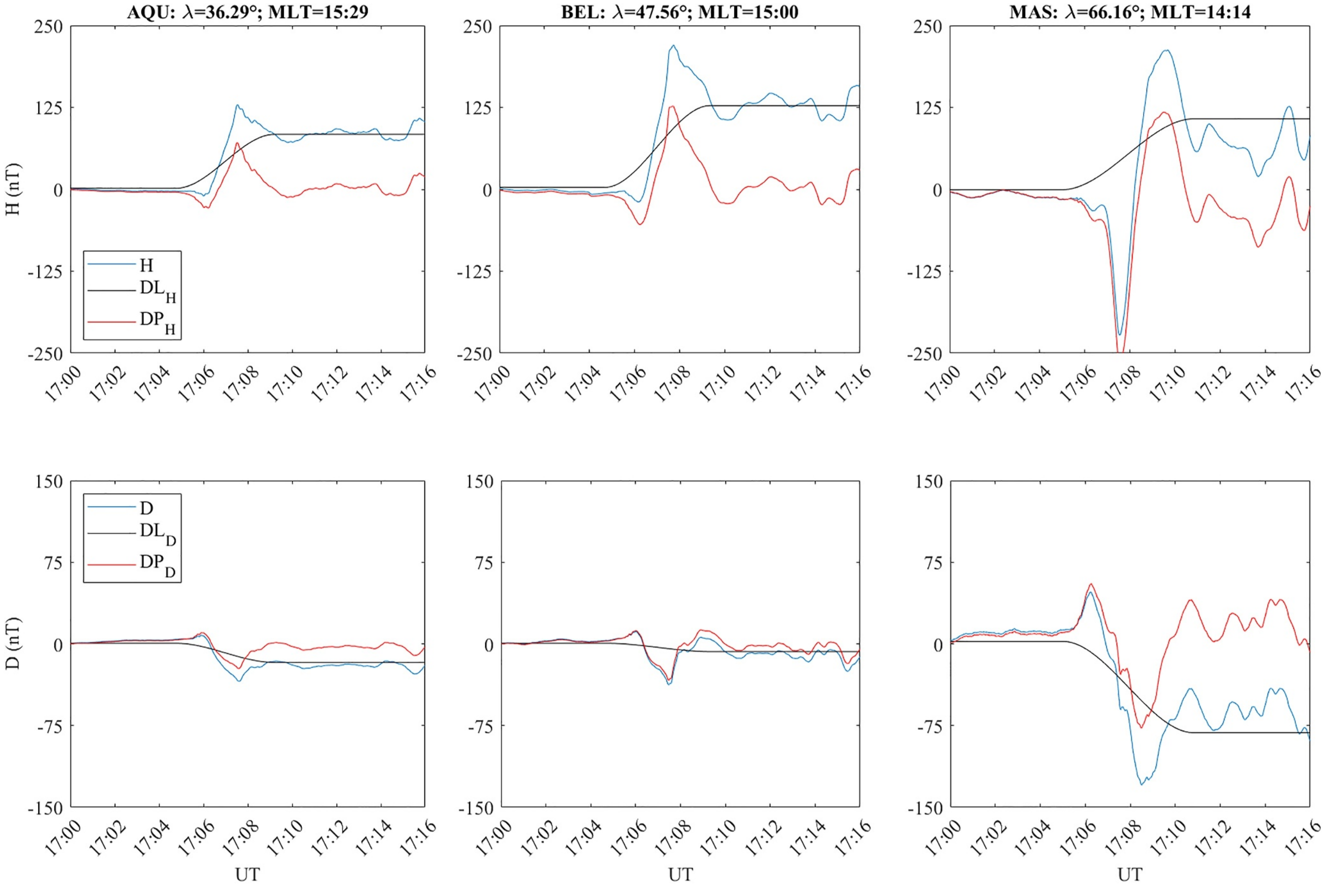

Figure 6. Magnetic field observations at three sample EMMA stations during the SSC occurrence. Upper panels show the H component, while lower panels show the D component. Plots from left to right are relative to L'Aquila (Italy, $\lambda = 36.29°$, $MLT = 15:29$), Belsk (Poland, $\lambda = 47.56°$, MLT = 15:00) and Masi (Finland, $\lambda = 66.16°$, MLT = 14:14) observatories, respectively. Black and red traces are representative of the magnetospheric and ionospheric SSC contribution, respectively.

Tozzi et al., 2019). In addition, the east-west component of the geoelectric field (E_D) shows larger amplitude variations than the north-south component (E_H).

To improve our understanding of the E amplitude variation as a function of magnetic latitude, we evaluated its variation between the 5 min averages before and after the SSC, corresponding to −16:58–17:03 UT and 17:11–17:16 UT time intervals, respectively. The results are reported in Figure 9. According to Marshall et al. (2010), who evaluated a similar parameter called GIC index, the amplitude of both E_H and E_D (hereafter GIE_H and GIE_D, respectively; GIE being the geomagnetically induced electric field) increases with magnetic latitude up to ∼62° when it falls down to lower values. In agreement with Tozzi et al. (2019), this behavior can be explained in terms of FAC effects that generate the most visible signature in the east-west component (e.g., Fujita, Tanaka, Kikuchi, Fujimoto, Hosokawa, & Itonaga, 2003; Fujita, Tanaka, Kikuchi, Fujimoto, & Itonaga, 2003; Kubota et al., 2015; Tanaka et al., 2020; Yu & Ridley, 2009; T. Zhang et al., 2023).

Figure 10 shows a map of geoelectric field variations for the SSC (17:05 UT). It can be easily seen that the highest GIE (and hence GIC) occurred at geographic latitudes $63° < \lambda < 69°$, in agreement with Carter et al. (2016) and Piersanti et al. (2019).

6. Discussion

Geomagnetic field variations occurring in the near-Earth space environment lead to the generation of a surface geoelectric field through the electromagnetic induction process, as reported by Viljanen and Pirjola (1994) and later by Pirjola (2000). This generated geoelectric field is critical as it drives GICs, posing a formidable challenge to modern society, especially given our increasing reliance on a stable and uninterrupted electricity supply

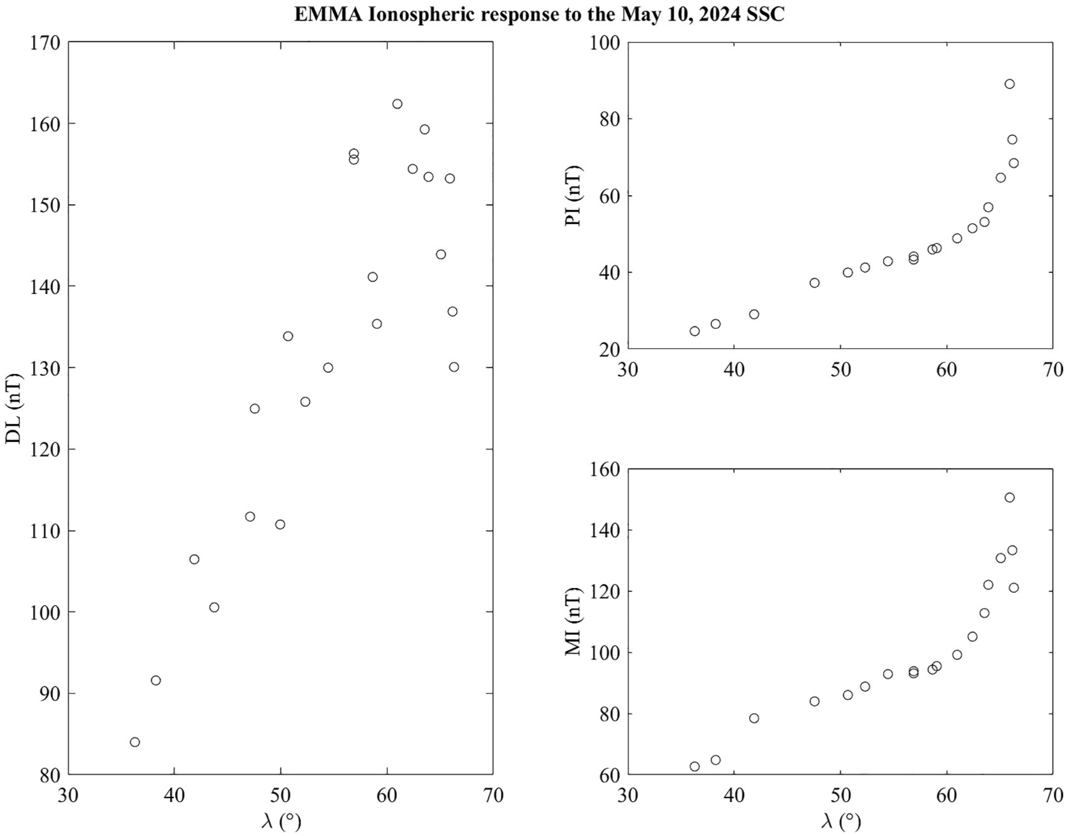

Figure 7. Amplitude of the DL (left panel) and DP (right panels) field as a function of the magnetic latitude along EMMA array. The DP field has been divided into the PI (upper right panel) and MI (lower right panel) contribution.

(Knipp, 2015). Understanding these dynamics is essential for developing effective strategies to mitigate risks associated with GICs, thus ensuring the resilience and reliability of our electrical infrastructure against natural electromagnetic disturbances.

Research has increasingly focused on quantifying and modeling the effects of GICs in high-latitude regions, particularly beneath auroral electrojets, where they exhibit their highest intensity. However, studies are revealing that equatorial latitudes also play a crucial role, with the equatorial electrojet (EEJ) suspected of significantly contributing to GIC generation and their dB/dt space weather driver during geomagnetic storms. In particular, findings by Carter et al. (2016) and Oliveira et al. (2018) highlight that dB/dt and GIC activity at equatorial latitudes peaks during solar events and interplanetary shock arrivals, even in the absence of a geomagnetic storm. This underscores the importance of understanding GIC dynamics across different latitudes, which is essential for developing effective monitoring and mitigation strategies in our increasingly technology-dependent society.

This analysis focuses on the magnetospheric and ground (over Europe) response, in terms of ionospheric current and GIC, to the passage of the interplanetary shock preceding the 10 May 2024 geomagnetic storm. The IPs was clearly detected by the DSCOVR satellite located at the L1 point as a sudden increase of all the SW parameters and IMF amplitude. The shock impact and the clock angle values, computed using the RH conditions, reveal a moderate inclination with respect to the GSE x-line ($\theta_{x_n} = 142.04°$) and more pronounced inclination with respect to the meridian GSE xz plane $\left(\varphi_{yb} = 96.64°\right)$. This unusual shock inclination in the meridian GSE xz plane led the IPs to impact the northern magnetosphere first, causing a large north-south asymmetry in the SSC response on the ground (see Figure 4), characterized by higher amplitudes in the northern hemisphere than in the southern hemisphere, except in the local noon. A possible explanation for a higher response in the southern hemisphere near noon is presumably due to weak magnitudes of the geomagnetic field that characterize the SAA (Trindade et al., 2018), hence leading to a higher relative response in the south. However, such a hypothesis can only be confirmed by statistical investigations. Furthermore, Xu et al. (2020) showed that stations with higher

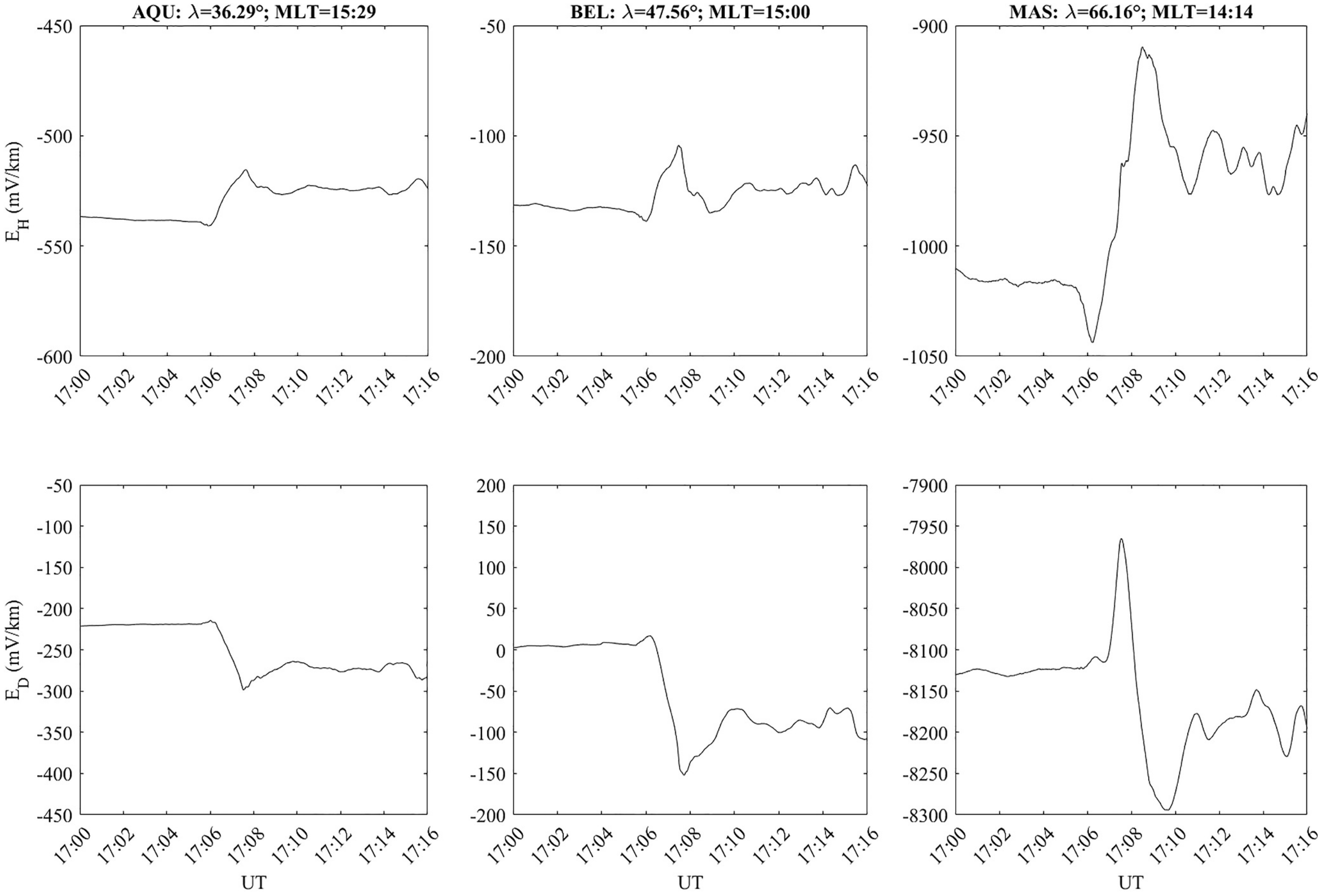

Figure 8. Geoelectric field as modeled by MA.I.GIC. model for three sample station of EMMA array. Upper and lower panels shows the E_H and E_D components, respectively. Left panels) Geoelectric field components modeled at L'Aquila (AQU, $\lambda = 36.39°$; MLT = 15:29); central panels) Geoelectric field components modeled at Belsk (BEL, $\lambda = 47.56°$; MLT = 15:00); right panels) Geoelectric field components modeled at Masi (MAS $\lambda = 66.16°$; MLT = 14:14).

ground dB/dt variations following shock impacts are located in the magnetospheric hemisphere that was first impacted by the shock.

In the magnetosphere, in agreement with statistical results by Villante and Piersanti (2008), the SSC was characterized by a strong sudden increase of the magnetopause and ring currents, as highlighted by the direct comparison between GOES$_{18}$ (located at 08:07 LT) observations and TS04* model prevision (see Figure 3 right panels). Concerning the ring current contribution, the separate analysis of both the symmetric and partial ring current showed that the latter only gives a small amplitude boost (∼2 nT) to the TS04* model predictions of the magnetospheric variation induced by the IPs arrival. This could be explained in terms of the different timescales of the partial and symmetric ring current injection. Indeed, as reported by Alberti et al. (2020), the partial ring current presents peculiar dynamics characterized by timescales longer than 10 min, corresponding to the 10 May 2024 SSC time duration. Regarding GOES$_{16}$, located around local noon, the same TS04* configuration was unable to reproduce magnetic field observations (see Figure 3 left panels). This can be due to the peculiar SW parameters (Figure 1) associated with the IPs that moved the standoff position of the magnetopause inward (Bonde et al., 2018) to a distance lower than the radius of the geosynchronous orbit (<6.5 Earth radii) leaving GOES$_{16}$ orbiting out of the magnetosphere. Our results are supported by the findings of Hayakawa et al. (2024), who reported of a significant inward morion of the magnetopause standoff position following the shock impact on 10 May 2024 at 17:05 UT.

On the ground, applying the Piersanti and Villante (2016) model, we evaluated both the DL (magnetospheric origin) and DP fields (ionospheric origin) along the EMMA array. In agreement with Araki (1994) and Piersanti and Villante (2016), we found that the DL field is characterized by a positive (negative) variation of the H (D)

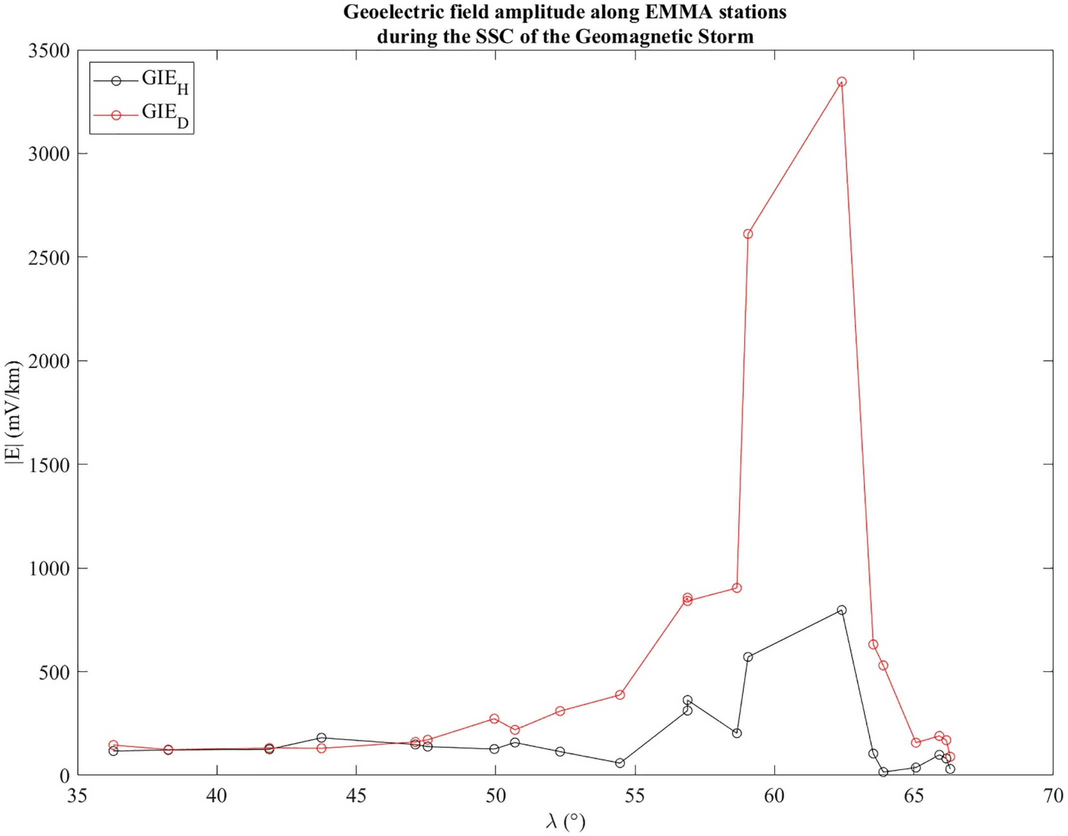

Figure 9. Geoelectric field amplitude as a function of the magnetic latitude for the EMMA array observed during the SSC. Red lines are representative of the E_D component, while black line are representative of the E_H component. Circles indicate the latitudinal location of each EMMA ground station.

component within 5 min between two steady states (Figure 6 black lines). The DL amplitude (Figure 7) increases with magnetic latitude up to ∼62° and then decreases. In general, the DL field, when generated by the magnetopause current alone, is expected to decrease with magnetic latitudes (Araki, 1994; Tsunomura, 1998; Villante & Piersanti, 2012). In some case events, its contribution is able to expand up to mid magnetic latitudes because of the concurring contribution of magnetopause and ring currents (symmetric and asymmetric part) on the dayside and of magnetopause and tail current, on the nightside (Piersanti & Villante, 2016; Shinbori et al., 2009; Vichare et al., 2014). In such an extreme event, because of the huge negative $B_{z,IMF}$ and high solar wind pressure value (see Figure 1), there were both an inward over-compression and an erosion of the magnetosphere (in fact, on the dayside GOES$_{16}$ crossed the magnetopause as reported in Figure 3). Such a peculiar condition would have driven the influence of the DL field up to mid/high magnetic latitudes. On the other hand, both the PI and the MI show amplitudes increasing with magnetic latitudes up to ∼65°. This result agrees with previous observations (e.g., Piersanti et al., 2017; Piersanti & Villante, 2016) and can be explained in terms of the DP-2 ionospheric current system (Piersanti & Villante, 2016; Shinbori et al., 2009; Tsunomura, 1998) switching on during the passage of the IP shock (Araki, 1994). A direct comparison with the June 2015 SSC amplitude (see Figure 39 in Piersanti et al., 2017) shows that, on average, the 10 May 2024 PI and MI amplitudes are 20% and 35% higher. Such intense geomagnetic (and hence geoelectric) field response observed when the EMMA array was near dusk local time is consistent with the superposed epoch analysis study of Madelaire et al. (2022b). Those authors showed that, in the noon/dusk sector, ground magnetic fields intensified nearly 30 min after solar wind ram pressure enhancements. Furthermore, Madelaire et al. (2022a) suggested that this preference for the duskside was associated with the generation of intense current vortices on the duskside, along with current vortices that traveled from dawn to dusk with significant speed. Madelaire et al. (2022a) attributed these effects to the intensification of the partial ring current, which is usually stronger in the dusk/midnight sector (De Michelis et al., 1997; Greenspan & Hamilton, 2000; Newell & Gjerloev, 2012). Additionally, Oliveira et al. (2024) reported on GIC enhancements in

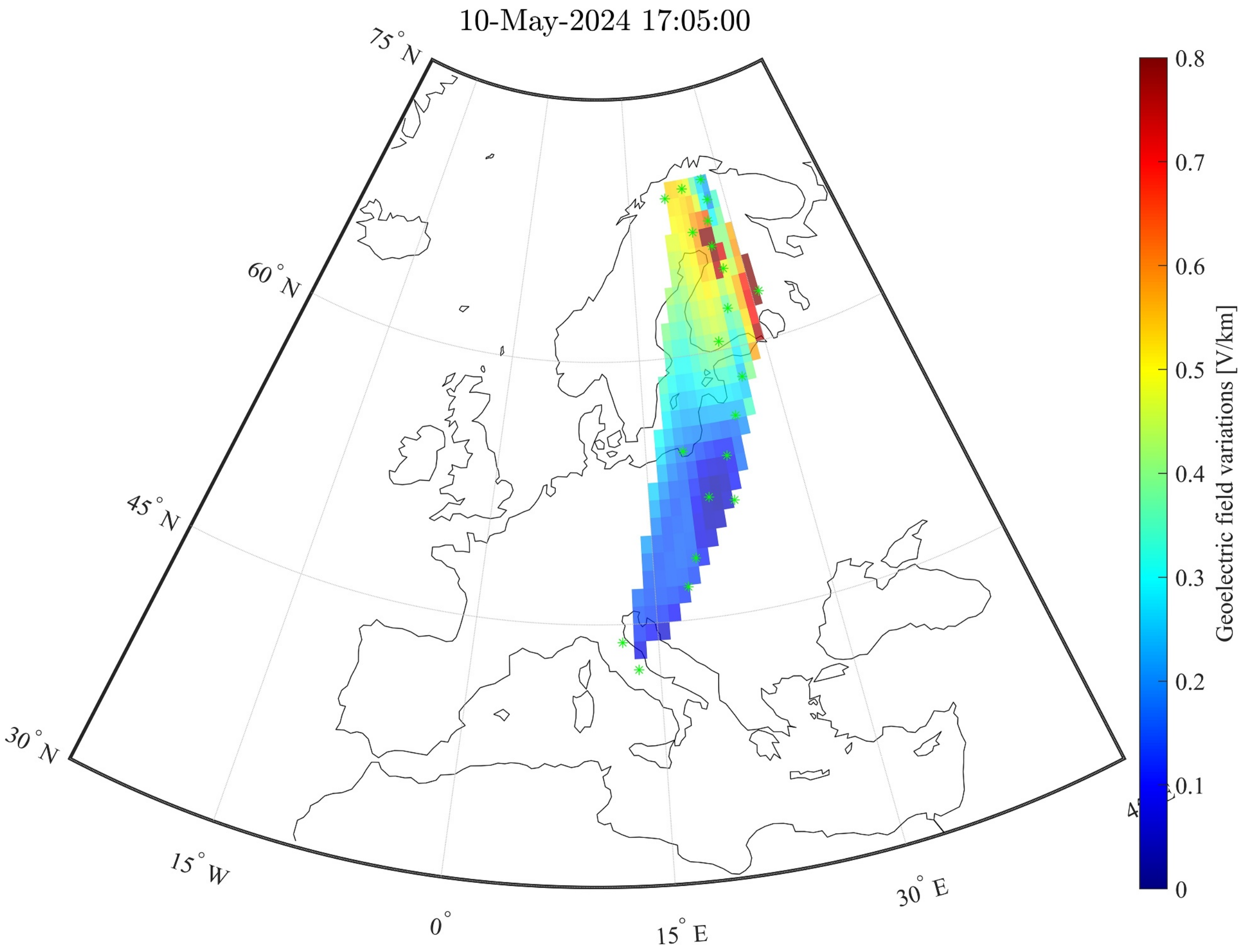

Figure 10. Geoelectric field maps over the EMMA array at the moment of the SSC occurrence.

southern Finland persistently occurring in the dusk sector within 20 min after shock impacts, particularly after nearly head-on impacts.

However, the peculiar inclination of the IP shock of 10 May 2024 caused GIE enhancements to be very localized at high latitudes. Oliveira and Raeder (2014) conducted numerical simulations of an IP shock with moderate inclination in the xz plane and no inclination in the xy plane (similar to our shock), and a purely frontal shock, to investigate the subsequent magnetosphere-ionosphere response to shock impacts. The authors concluded that the FAC response to the frontal case was stronger and reached lower latitudes compared to the inclined response, even though the frontal shock was weaker than the inclined shock. Oliveira and Raeder (2014) attributed these results to the more symmetric nature of magnetospheric compression by frontal shock which caused more rapid and stronger current enhancements compared to more gradual and weaker current enhancements by the inclined shock. The results shown in Figures 9 and 10 indicate that intense GIE response to the shock was mostly localized at magnetic latitudes in the range ~61°-63°. In general, simulation studies (e.g., Fujita et al., 2003a, 2003b; Kubota et al., 2015; Tanaka et al., 2020; Yu & Ridley, 2009; T. Zhang et al., 2023) showed that the strongest FAC system response is located at a magnetic latitude greater than 65°. However, being the Gannon SSC characterized by both strong Pd and high southward $B_{z,IMF}$, the FAC locations may be moved to lower magnetic latitudes than expected. Therefore, we suggest that, being the 10 May 2024 shock more frontal, the subsequent GIE response would have reached considerably lower magnetic latitudes, including northern Italian regions. As a result, we suggest that the shock impact angle may play a significant role for future predictions of GIE enhancements based on solar wind and IMF measurements at L1.

The significant SSC observed during this event was the main driver of GIEs. Our findings indicate that the highest GIE amplitudes (Figure 9) occur at magnetic latitudes above 62°. Moreover, the geoelectric field amplitude as a function of magnetic latitude (Figure 9) shows a similar behavior as the DL field (Figure 7 left panel), suggesting a non-negligible contribution of the magnetospheric current system in generating GIEs and hence GICs. This is confirmed by the behavior of the geoelectric field shown in Figure 8, where a clear step-like variation is superimposed on smaller time-scales fluctuation along both north-south and east-west components. Being the step-like variation directly related to the compressional wave driven by the IPs impinging onto the magnetosphere, we also suggest that there is a contribution of the magnetospheric field to GIEs during the SSC. This claim disagrees with previous studies (e.g., Boutsi et al., 2023; Carter et al., 2015; Espinosa et al., 2023; Marshall et al., 2010; Tozzi et al., 2019). A possible explanation lies in the different ways the GICs were estimated. In general, the literature estimates GIC effects using the $\frac{dB}{dt}$ approach (e.g., Boutsi et al., 2023; Carter et al., 2015, 2016). Moreover, the use of a technique based on a derivative of the magnetic field with time results in removing a longer time scale on a given signal (the derivative is similar to a high-pass filter) (Miao & Clements, 2002). In fact, magnetospheric field contribution, being characterized by longer time scales than ionospheric field, vanishes when the $\frac{dB}{dt}$ technique is used. On the other hand, the geoelectric field, being directly related to magnetic field observations via the magnetotelluric equation (Piersanti et al., 2019, and reference therein), can be used to evaluate whether magnetospheric current systems could play a role in driving the GIC amplitude. Specifically, for the present event, the direct comparison between magnetospheric field observations and TS04* model predictions confirms that the SSC amplitude was driven by the concurring contribution of the magnetopause and ring currents (Araki, 1994; Villante & Piersanti, 2012) (see Figure 3). On the other hand, the geoelectric field behavior (Figure 8), similar to the magnetic field observations, shows rapid variations (between 1 and 3 min) that can be directly linked to the DP field, namely to the ionospheric current. As a consequence, we could reasonably say that, at ground, the GIE, and hence GIC behavior, during a SSC would be driven by both ionospheric field whose variations are characterized by timescales between 1 and 4 min, and magnetospheric currents whose variations are characterized by timescales greater than 5 min (each timescale was evaluated averaging the duration of the DP and DL fields for the entire EMMA array, respectively). The magnetospheric origin variation identified in the calculated GIEs is responsible for sudden changes of the GIE baseline, which, in turn, would drive sudden variation of GICs. To confirm such a hypothesis, we will perform a statistical analysis of SSC and Sudden Impulses whose results will be presented in a forthcoming paper.

7. Conclusions

In today's increasingly technological society, understanding space weather is crucial for safeguarding critical infrastructure, both in space and on Earth. The impact of space weather, particularly during periods of high solar activity, can significantly affect the evolution of the IMF as it interacts with our planet. This interaction leads to variations in electric currents flowing through the magnetosphere-ionosphere system and at ground level, which can disrupt power grids and telecommunications, posing risks to everyday life (Pulkkinen, 2015). By prioritizing space weather predictions and their implications, we can enhance our readiness and resilience against these natural phenomena, ensuring the stability of essential services and the safety of technological systems.

The present work demonstrates that high GIC values are influenced not only by geomagnetic storms but also by IPs impacting the magnetopause. Additionally, the strong correlation between the GIC amplitude and the SSC currents amplitude confirms the direct cause-and-effect relationship between magnetospheric-ionospheric current amplification and GIC production. In addition, our results on GIE amplitude variations as a function of magnetic latitude and GIE behavior suggest that, during SSCs, GIEs could not be driven by ionospheric currents alone, but also by magnetospheric currents. The former, being directly driven by the injection of an Alfvén wave in the magnetosphere during the passage of IPs (Araki, 1994), would be responsible for time-scale variations in the range of 1–3 min, The magnetospheric origin contribution, being directly related to the compressional wave associated with the IPS, are characterized by longer time-scales and would be responsible for a change into the baseline of GIEs, and hence GICs.

Data Availability Statement

DSCOVR (NOAA-DSCOVR, 2016) and GOES (NOAA-GOES, 1994) satellite data are freely available from the NASA-CDAWEB data service. INTERMAGNET geomagnetic field data are freely available at

INTERMAGNET website (INTERMAGNET, 2024). EMMA data (Piersanti, 2024) used in this study are available from Zenodo. The global conductivity model used in the evaluation of the geoelectric field (Piersanti et al., 2019) is available from Alekseev et al. (2019) in either MATLAB or text formats. Geomagnetic and solar indices from SuperMAG data set are freely available at SuperMAG website (Gjerloev, 2012). The software to evaluate the magnetospheric model by N. A. Tsyganenko and Sitnov (2005) and the GEOPACK 2008 library are openly available N. Tsyganenko and Andreeva (2022) website.

Acknowledgments

DSCOVR data were obtained from the NOAA's National Centers for Environmental Information (NCEI) Data Center. We thank the national institutes that support INTERMAGNET data for promoting high standards of magnetic observatory practice (www.intermagnet.org). We acknowledge use of NOAA Space Weather Prediction Center for obtaining GOES magnetometer data. We thank the Finnish Meteorological Institute (FMI), the University of Oulu (Finland), the Institute of Geophysics of the Polish Academy of Sciences (IGF-PAS), the Mining and Geological Survey of Hungary, and the University of L'Aquila for contributing to EMMA. DMO acknowledges financial support provided by NASA's Heliophysics Guest Investigator Open program (Grant 80NSSC22K0756). MP, GdA, and PD thank the Italian Space Agency for the financial support under the contract ASI "LIMADOU scienza+" no 2021-18-H1. Open access publishing facilitated by Istituto nazionale di astrofisica, as part of the Wiley - CRUI-CARE agreement.

References

Alberti, T., Lekscha, J., Consolini, G., Michelis, D., & Donner, R. V. (2020). Disentangling nonlinear geomagnetic variability during magnetic storms and quiescence by timescale dependent recurrence properties. *Journal of Space Weather and Space Climate*, *10*, 25. https://doi.org/10.1051/swsc/2020026

Alekseev, D., Alexey, K., & Nikolay, P. (2019). *Compilation of 3-D global conductivity model of the earth for space weather and other applications*. P.P Shirshov Institute of Oceanology Russian Academy of Sciences. Retrieved from https://globalconductivity.ocean.ru/index.html

Araki, T. (1977). Global structure of geomagnetic sudden commencements. *Planetary and Space Science*, *25*(4), 373–384. https://doi.org/10.1016/0032-0633(77)90053-8

Araki, T. (1994). A Physical model of the geomagnetic sudden commencement. *Geophysical Monograph Series*, *81*, 183–200. https://doi.org/10.1029/GM081p0183

Araki, T., & Shinbori, A. (2016). Relationship between solar wind dynamic pressure and amplitude of geomagnetic sudden commencement (SC). *Earth Planets and Space*, *68*, 1–7. https://doi.org/10.1186/s40623-016-0444-y

Bonde, R. E. F., Lopez, R. E., & Wang, J. Y. (2018). The effect of IMF fluctuations on the subsolar magnetopause position: A study using a global MHD model. *Journal of Geophysical Research: Space Physics*, *123*(4), 2598–2604. https://doi.org/10.1002/2018JA025203

Boudouridis, A., Zesta, E., Lyons, R., Anderson, P., & Lummerzheim, D. (2003). Effect of solar wind pressure pulses on the size and strength of the auroral oval. *Journal of Geophysical Research*, *108*(A4), 8012. https://doi.org/10.1029/2002ja009373

Boutsi, A. Z., Balasis, G., Dimitrakoudis, S., Daglis, I. A., Tsinganos, K., Papadimitriou, C., & Giannakis, O. (2023). Investigation of the geomagnetically induced current index levels in the Mediterranean region during the strongest magnetic storms of solar cycle 24. *Space Weather*, *21*(2), e2022SW003122. https://doi.org/10.1029/2022SW003122

Carter, B. A., Yizengaw, E., Pradipta, R., Halford, A. J., Norman, R., & Zhang, K. (2015). Interplanetary shocks and the resulting geomagnetically induced currents at the equator. *Geophysical Research Letters*, *42*(16), 6554–6559. https://doi.org/10.1002/2015gl065060

Carter, B. A., Yizengaw, E., Pradipta, R., Weygand, J. M., Piersanti, M., Pulkkinen, A., et al. (2016). Geomagnetically induced currents around the world during the 17 March 2015 storm. *Journal of Geophysical Research: Space Physics*, *121*(10), 10496–10507. https://doi.org/10.1002/2016JA023344

Crooker, N., Joselyn, J. A., & Feynman, J. (1997). Coronal mass ejections. *Geophysical Monograph Series*, *99*. https://doi.org/10.1029/GM099

De Michelis, P., Daglis, I. A., & Consolini, G. (1997). Average terrestrial ring current derived from AMPTE/CCE-CHEM measurements. *Journal of Geophysical Research*, *102*(A7), 14103–14111. https://doi.org/10.1029/96JA03743

Espinosa, K. V., Padilha, A. L., Alves, L. R., Schultz, A., & Kelbert, A. (2023). Estimating geomagnetically induced currents in southern Brazil using 3-D earth resistivity model. *Space Weather*, *21*(4), e2022SW003166. https://doi.org/10.1029/2022SW003166

Feldstein, Y. I., Grafe, A., Gromova, L., & Popov, V. (1997). Auroral electrojets during geomagnetic storms. *Journal of Geophysical Research*, *102*(A7), 14223–14235. https://doi.org/10.1029/97ja00577

Fujita, S., Tanaka, T., Kikuchi, T., Fujimoto, K., Hosokawa, K., & Itonaga, M. (2003a). A numerical simulation of the geomagnetic sudden commencement: 1. Generation of the field-aligned current associated with the preliminary impulse. *Journal of Geophysical Research*, *108*(A12). https://doi.org/10.1029/2002JA009407

Fujita, S., Tanaka, T., Kikuchi, T., Fujimoto, K., & Itonaga, M. (2003b). A numerical simulation of the geomagnetic sudden commencement: 2. Plasma processes in the main impulse. *Journal of Geophysical Research*, *108*(A12), 1417. https://doi.org/10.1029/2002JA009763

Gjerloev, J. W. (2009). A global ground-based magnetometer initiative. *Eos Transactions AGU*, *90*(27), 230–231. https://doi.org/10.1029/2009EO270002

Gjerloev, J. W. (2012). The SuperMAG data processing technique. *Journal of Geophysical Research*, *117*(A09213), 1–19. https://doi.org/10.1029/2012JA017683

Gonzalez, W., Joselyn, J.-A., Kamide, Y., Kroehl, H. W., Rostoker, G., Tsurutani, B., & Vasyliunas, V. (1994). What is a geomagnetic storm? *Journal of Geophysical Research*, *99*(A4), 5771–5792. https://doi.org/10.1029/93ja02867

Gonzalez, W. D., Tsurutani, B. T., & Clúa de Gonzalez, A. L. (1999). Interplanetary origin of geomagnetic storms. *Space Science Reviews*, *88*(3), 529–562. https://doi.org/10.1023/a:1005160129098

Greenspan, M. E., & Hamilton, D. C. (2000). A test of the Dessler-Parker-Sckopke relation during magnetic storms. *Journal of Geophysical Research*, *105*(A3), 5419–5430. https://doi.org/10.1029/1999JA000284

Hayakawa, H., Ebihara, Y., Mishev, A., Koldobskiy, S., Kusano, K., Bechet, S., et al. (2024). The solar and geomagnetic storms in May 2024: A flash data report. *The Astrophysical Journal*, *979*(1), 49. https://doi.org/10.3847/1538-4357/ad9335

Iijima, T., & Potemra, T. A. (1976). The amplitude distribution of field-aligned currents at northern high latitudes observed by Triad. *Journal of Geophysical Research*, *81*(13), 2165–2174. https://doi.org/10.1029/JA081i013p02165

INTERMAGNET, e. a. (2024). Intermagnet reference data set (IRDS) 2020 – Definitive magnetic observatory data. *GFZ Data Services*. https://doi.org/10.5880/INTERMAGNET.1991.2020

Kennel, C. F., Blandford, R. D., & Coppi, P. (1989). MHD intermediate shock discontinuities. Part 1. Rankine-Hugoniot conditions. *Journal of Plasma Physics*, *42*(2), 299–319. https://doi.org/10.1017/S0022377800014379

Knipp, D. J. (2015). Synthesis of geomagnetically induced currents: Commentary and research. *Space Weather*, *13*(11), 727–729. https://doi.org/10.1002/2015SW001317

Kubota, Y., Kataoka, R., Den, M., Tanaka, T., Nagatsuma, T., & Fujita, S. (2015). Global MHD simulation of magnetospheric response of preliminary impulse to large and sudden enhancement of the solar wind dynamic pressure. *Earth Planets and Space*, *67*, 1–9. https://doi.org/10.1186/s40623-015-0270-7

Laundal, K. M., & Richmond, A. D. (2017). Magnetic coordinate systems. *Space Science Reviews*, *206*(1), 27–59. https://doi.org/10.1007/s11214-016-0275-y

Lee, D.-Y., & Lyons, L. (2004). Geosynchronous magnetic field response to solar wind dynamic pressure pulse. *Journal of Geophysical Research*, *109*(A4), A04201. https://doi.org/10.1029/2003ja010076

Lichtenberger, J., Clilverd, M. A., Heilig, B., Vellante, M., Manninen, J., Rodger, C. J., et al. (2013). The plasmasphere during a space weather event: First results from the Plasmon project. *Journal of Space Weather and Space Climate*, *3*, A23. https://doi.org/10.1051/swsc/2013045

Liu, C., Ganebo, Y. S., Wang, H., & Li, X. (2018). Geomagnetically induced currents in Ethiopia power grid: Calculation and analysis. *IEEE Access*, *6*, 64649–64658. https://doi.org/10.1109/access.2018.2877618

Lockwood, M., McWilliams, K. A., Owens, M. J., Barnard, L. A., Watt, C. E., Scott, C. J., et al. (2020). Semi-annual, annual and universal time variations in the magnetosphere and in geomagnetic activity: 2. Response to solar wind power input and relationships with solar wind dynamic pressure and magnetospheric flux transport. *Journal of Space Weather and Space Climate*, *10*, 30. https://doi.org/10.1051/swsc/2020033

Loto'aniu, P. T. M., Romich, K., Rowland, W., Codrescu, S., Biesecker, D., Johnson, J., et al. (2022). Validation of the DSCOVR spacecraft mission space weather solar wind products. *Space Weather*, *20*(10), e2022SW003085. https://doi.org/10.1029/2022SW003085

Loto'aniu, T., Davis, A., Jarvis, A., Grotenhuis, M., Rich, F., Califf, S., et al. (2023). Initial on-orbit results from the goes-18 spacecraft science magnetometer. *Space Science Reviews*, *219*(8), 84. https://doi.org/10.1007/s11214-023-01032-3

Loto'aniu, T., Redmon, R., Califf, S., Singer, H., Rowland, W., Macintyre, S., et al. (2019). The goes-16 spacecraft science magnetometer. *Space Science Reviews*, *215*(4), 1–28. https://doi.org/10.1007/s11214-019-0600-3

Loto'aniu, T. M., Singer, H. J., Rodriguez, J. V., Green, J., Denig, W., Biesecker, D., & Angelopoulos, V. (2015). Space weather conditions during the Galaxy 15 spacecraft anomaly. *Space Weather*, *13*(8), 484–502. https://doi.org/10.1002/2015SW001239

Lugaz, N., Farrugia, C. J., Smith, C. W., & Paulson, K. (2015). Shocks inside CMES: A survey of properties from 1997 to 2006. *Journal of Geophysical Research: Space Physics*, *120*(4), 2409–2427. https://doi.org/10.1002/2014ja020848

Mac Manus, D. H., Rodger, C. J., Dalzell, M., Thomson, A. W., Clilverd, M. A., Petersen, T., et al. (2017). Long-term geomagnetically induced current observations in New Zealand: Earth return corrections and geomagnetic field driver. *Space Weather*, *15*(8), 1020–1038. https://doi.org/10.1002/2017sw001635

Madelaire, M., Laundal, K. M., Reistad, J. P., Hatch, S. M., & Ohma, A. (2022a). Transient high latitude geomagnetic response to rapid increases in solar wind dynamic pressure. *Frontiers in Astronomy and Space Sciences*, *9*. https://doi.org/10.3389/fspas.2022.953954

Madelaire, M., Laundal, K. M., Reistad, J. P., Hatch, S. M., Ohma, A., & Haaland, S. (2022b). Geomagnetic response to rapid increases in solar wind dynamic pressure: Event detection and large scale response. *Frontiers in Astronomy and Space Sciences*, *9*, 904620. https://doi.org/10.3389/fspas.2022.904620

Marshall, R. A., Kelly, A., Van Der Walt, T., Honecker, A., Ong, C., Mikkelsen, D., et al. (2017). Modeling geomagnetic induced currents in Australian power networks. *Space Weather*, *15*(7), 895–916. https://doi.org/10.1002/2017sw001613

Marshall, R. A., Waters, C. L., & Sciffer, M. D. (2010). Spectral analysis of pipe-to-soil potentials with variations of the earth's magnetic field in the Australian region. *Space Weather*, *8*(5). https://doi.org/10.1029/2009SW000553

Matsushita, S. (1962). On geomagnetic sudden commencements, sudden impulses, and storm durations. *Journal of Geophysical Research*, *67*(10), 3753–3777. https://doi.org/10.1029/jz067i010p03753

Miao, G. J., & Clements, M. A. (2002). *Digital signal processing and statistical classification*. Artech House.

Newell, P. T., & Gjerloev, J. W. (2011). Evaluation of SuperMAG auroral electrojet indices as indicators of substorms and auroral power. *Journal of Geophysical Research*, *116*(A12), A12211. https://doi.org/10.1029/2011JA016779

Newell, P. T., & Gjerloev, J. W. (2012). SuperMAG-based partial ring current indices. *Journal of Geophysical Research*, *117*(A05215), 1–15. https://doi.org/10.1029/2012JA017586

Ngwira, C. M., Pulkkinen, A., Wilder, F. D., & Crowley, G. (2013). Extended study of extreme geoelectric field event scenarios for geomagnetically induced current applications. *Space Weather*, *11*(3), 121–131. https://doi.org/10.1002/swe.20021

Ngwira, C. M., Pulkkinen, A. A., Bernabeu, E., Eichner, J., Viljanen, A., & Crowley, G. (2015). Characteristics of extreme geoelectric fields and their possible causes: Localized peak enhancements. *Geophysical Research Letters*, *42*(17), 6916–6921. https://doi.org/10.1002/2015gl065061

NOAA-DSCOVR. (2016). *Deep space climate observatory (DSCOVR)*. NOAA National Centers for Environmental Information. https://doi.org/10.7289/V51Z42F7

NOAA-GOES. (1994). *Noaa geostationary operational environmental satellite (GOES) I-M and N-P series imager data*. NOAA National Centers for Environmental Information. https://doi.org/10.25921/Z9JQ-K976

Oliveira, D. M. (2023a). Geoeffectiveness of interplanetary shocks controlled by impact angles: Past research, recent advancements, and future work. *Frontiers in Astronomy and Space Sciences*, *10*. https://doi.org/10.3389/fspas.2023.1179279

Oliveira, D. M. (2023b). Interplanetary shock data base. *Frontiers in Astronomy and Space Sciences*, *10*, 1240323. https://doi.org/10.3389/fspas.2023.1240323

Oliveira, D. M., Arel, D., Raeder, J., Zesta, E., Ngwira, C. M., Carter, B. A., et al. (2018). Geomagnetically induced currents caused by interplanetary shocks with different impact angles and speeds. *Space Weather*, *16*(6), 636–647. https://doi.org/10.1029/2018SW001880

Oliveira, D. M., & Raeder, J. (2014). Impact angle control of interplanetary shock geoeffectiveness. *Journal of Geophysical Research: Space Physics*, *119*(10), 8188–8201. https://doi.org/10.1002/2014JA020275

Oliveira, D. M., Zesta, E., & Vidal-Luengo, S. (2024). First direct observations of interplanetary shock impact angle effects on actual geomagnetically induced currents: The case of the Finnish natural gas pipeline system. *Frontiers in Astronomy and Space Sciences*, *11*. https://doi.org/10.3389/fspas.2024.1392697

Olson, J. V., & Lee, L. (1983). Pc1 wave generation by sudden impulses. *Planetary and Space Science*, *31*(3), 295–302. https://doi.org/10.1016/0032-0633(83)90079-X

Piersanti, M. (2024). Emma data during the SSC of May 10, 2024 storm. *Zenodo*. https://doi.org/10.5281/zenodo.13891318

Piersanti, M., Alberti, T., Bemporad, A., Berrilli, F., Bruno, R., Capparelli, V., et al. (2017). Comprehensive analysis of the geoeffective solar event of 21 June 2015: Effects on the magnetosphere, plasmasphere, and ionosphere systems. *Solar Physics*, *292*(11), 169. https://doi.org/10.1007/s11207-017-1186-0

Piersanti, M., Del Moro, D., Parmentier, A., Martucci, M., Palma, F., Sotgiu, A., et al. (2022). On the magnetosphere-ionosphere coupling during the May 2021 geomagnetic storm. *Space Weather*, *20*(6), e2021SW003016. https://doi.org/10.1029/2021SW003016

Piersanti, M., Di Matteo, S., Carter, B., Currie, J., & D'Angelo, G. (2019). Geoelectric field evaluation during the September 2017 geomagnetic storm: Ma. I. GIC. Model. *Space Weather*, *17*(8), 1241–1256. https://doi.org/10.1029/2019sw002202

Piersanti, M., & Villante, U. (2016). On the discrimination between magnetospheric and ionospheric contributions on the ground manifestation of sudden impulses. *Journal of Geophysical Research: Space Physics*, *121*(7), 6674–6691. https://doi.org/10.1002/2015JA021666

Pirjola, R. (2000). Geomagnetically induced currents during magnetic storms. *IEEE Transactions on Plasma Science*, *28*(6), 1867–1873. https://doi.org/10.1109/27.902215

Pirjola, R. (2002). Review on the calculation of surface electric and magnetic fields and of geomagnetically induced currents in ground-based technological systems. *Surveys in Geophysics*, *23*(1), 71–90. https://doi.org/10.1023/a:1014816009303

Priest, E. F. (1981). *Solar magnetohydrodynamics*. D. Reidel Publishing.

Pulkkinen, A. (2015). Geomagnetically Induced currents modeling and forecasting. *Space Weather*, *13*(11), 734–736. https://doi.org/10.1002/2015SW001316

Pulkkinen, A., Bernabeu, E., Eichner, J., Beggan, C., & Thomson, A. (2012). Generation of 100-year geomagnetically induced current scenarios. *Space Weather*, *10*(4), S04003. https://doi.org/10.1029/2011sw000750

Rastogi, R. G. (1978). Theory for preliminary negative impulse in storm sudden commencement in H at equatorial stations. *Indian Academy of Sciences Proceedings Section A*, *87*(3), 57–60. https://doi.org/10.1007/bf02839385

Rodger, C. J., Mac Manus, D. H., Dalzell, M., Thomson, A. W., Clarke, E., Petersen, T., et al. (2017). Long-term geomagnetically induced current observations from New Zealand: Peak current estimates for extreme geomagnetic storms. *Space Weather*, *15*(11), 1447–1460. https://doi.org/10.1002/2017sw001691

Shen, C., Chi, Y., Wang, Y., Xu, M., & Wang, S. (2017). Statistical comparison of the ICME's geoeffectiveness of different types and different solar phases from 1995 to 2014. *Journal of Geophysical Research: Space Physics*, *122*(6), 5931–5948. https://doi.org/10.1002/2016JA023768

Shinbori, A., Tsuji, Y., Kikuchi, T., Araki, T., & Watari, S. (2009). Magnetic latitude and local time dependence of the amplitude of geomagnetic sudden commencements. *Journal of Geophysical Research*, *114*(A4), A04217. https://doi.org/10.1029/2008JA013871

Souza, V. M., Koga, D., Gonzalez, W. D., & Cardoso, F. R. (2017). Observational aspects of magnetic reconnection at the earth's magnetosphere. *Brazilian Journal of Physics*, *47*(4), 447–459. https://doi.org/10.1007/s13538-017-0514-z

St-Louis, B. (Ed.) (2020). INTERMAGNET: Technical reference manual, *INTERMAGNET operations committee and executive council (Version 5.0.0)*. British Geological Survey.

Tanaka, T., Ebihara, Y., Watanabe, M., Den, M., Fujita, S., Kikuchi, T., et al. (2020). Reproduction of ground magnetic variations during the SC and the substorm from the global simulation and Biot-Savart's law. *Journal of Geophysical Research: Space Physics*, *125*(2), e2019JA027172. https://doi.org/10.1029/2019JA027172

Tozzi, R., De Michelis, P., Coco, I., & Giannattasio, F. (2019). A preliminary risk assessment of geomagnetically induced currents over the Italian territory. *Space Weather*, *17*(1), 46–58. https://doi.org/10.1029/2018SW002065

Trindade, R. I. F., Jaqueto, P., Terra-Nova, F., Brandt, D., Hartmann, G. A., Feinberg, J. M., et al. (2018). Speleothem record of geomagnetic south Atlantic anomaly recurrence. *Proceedings of the National Academy of Sciences*, *115*(52), 13198–13203. https://doi.org/10.1073/pnas.1809197115

Tsunomura, S. (1998). Characteristics of geomagnetic sudden commencement observed in middle and low latitudes. *Earth Planets and Space*, *50*(9), 755–772. https://doi.org/10.1186/bf03352168

Tsurutani, B., Zhou, X.-Y., Arballo, J., Gonzalez, W., Lakhina, G., Vasyliunas, V., et al. (2001). Auroral zone dayside precipitation during magnetic storm initial phases. *Journal of Atmospheric and Solar-Terrestrial Physics*, *63*(5), 513–522. https://doi.org/10.1016/s1364-6826(00)00161-9

Tsyganenko, N., & Andreeva, V. (2022). Modeling the earth's magnetosphere using spacecraft magnetometer data. *Russian Foundation for Basic Research (RFBR) grant 20-05-00218*. Retrieved from https://geo.phys.spbu.ru/~tsyganenko/empirical-models/

Tsyganenko, N. A., & Sitnov, M. I. (2005). Modeling the dynamics of the inner magnetosphere during strong geomagnetic storms. *Journal of Geophysical Research*, *110*(A3), A03208. https://doi.org/10.1029/2004JA010798

Vellante, M., Piersanti, M., Heilig, B., Reda, J., & Del Corpo, A. (2014). Magnetospheric plasma density inferred from field line resonances: Effects of using different magnetic field models. In *2014 XXXIth URSI general assembly and scientific symposium (URSI GASS)* (pp. 1–4). https://doi.org/10.1109/URSIGASS.2014.6929941

Vichare, G., Rawat, R., Bhaskar, A., & Pathan, B. M. (2014). Ionospheric current contribution to the main impulse of a negative sudden impulse. *Earth Planets and Space*, *66*(92), 1–21. https://doi.org/10.1186/1880-5981-66-92

Viljanen, A., & Pirjola, R. (1994). Geomagnetically induced currents in the Finnish high-voltage power system: A geophysical review. *Surveys in Geophysics*, *15*(4), 383–408. https://doi.org/10.1007/bf00665999

Viljanen, A., Pulkkinen, A., Amm, O., Pirjola, R., Korja, T., & Group, B. W. (2004). Fast computation of the geoelectric field using the method of elementary current systems and planar Earth models. *Annales Geophysicae*, *22*(1), 101–113. https://doi.org/10.5194/angeo-22-101-2004

Villante, U., & Piersanti, M. (2008). An analysis of sudden impulses at geosynchronous orbit. *Journal of Geophysical Research*, *113*(A8), A08213. https://doi.org/10.1029/2008JA013028

Villante, U., & Piersanti, M. (2009). Analysis of geomagnetic sudden impulses at low latitudes. *Journal of Geophysical Research*, *114*(A6), A06209. https://doi.org/10.1029/2008JA013920

Villante, U., & Piersanti, M. (2011). Sudden impulses at geosynchronous orbit and at ground. *Journal of Atmospheric and Solar-Terrestrial Physics*, *73*(1), 61–76. https://doi.org/10.1016/j.jastp.2010.01.008

Villante, U., & Piersanti, M. (2012). Sudden impulses in the magnetosphere and at ground. In M. Lazar (Ed.), *Exploring the solar wind (chap. 17)*. InTech. https://doi.org/10.5772/36770

Xu, Z., Hartinger, M. D., Oliveira, D. M., Coyle, S., Clauer, C. R., Weimer, D., & Edwards, T. (2020). Inter-hemispheric asymmetries in the ground magnetic response to interplanetary shocks: The role of shock impact angle. *Space Weather*, *18*(3), e2019SW002427. https://doi.org/10.1029/2019SW002427

Yu, Y., & Ridley, A. J. (2009). The response of the magnetosphere-ionosphere system to a sudden dynamic pressure enhancement under southward IMF conditions. *Annales Geophysicae*, *27*(12), 4391–4407. https://doi.org/10.5194/angeo-27-4391-2009

Zhang, D., Liu, W., Li, X., Sarris, T. E., Wang, Y., Xiao, C., et al. (2020). Relation between shock-related impulse and subsequent ULF wave in the Earth's magnetosphere. *Geophysical Research Letters*, *47*(23), e2020GL090027. https://doi.org/10.1029/2020GL090027

Zhang, T., Ebihara, Y., & Tanaka, T. (2023). Nighttime geomagnetic response to jumps of solar wind dynamic pressure: A possible cause of Québec blackout in March 1989. *Space Weather*, *21*(11), e2023SW003493. https://doi.org/10.1029/2023SW003493